ADVANCED FUNCTIONAL MATERIALS
www.afm-journal.de

Intelligent Magnetic Microrobots with Fluorescent Internal Memory for Monitoring Intragastric Acidity

*N. Senthilnathan, Cagatay M. Oral, Adam Novobilsky, and Martin Pumera**

This study investigates the dynamic fluctuations of pH caused by gastric acid secretion, a process of both biological and clinical significance, with microrobots. Abnormal patterns of acidity often indicate gastrointestinal diseases, underlying the importance of precise intragastric pH monitoring. Traditional methods using fluorescent probes face challenges due to their faint solid-state fluorescence, limited target specificity, and accuracy. To overcome these obstacles, pH-responsive fluorescent organic microparticles decorated with magnetite (Fe_3O_4) nanoparticles are engineered. These microrobots exhibit a unique fluorescence switching capability at a critical pH, enabling the monitoring of gastric acidity. The magnetic part of these microrobots ensures magnetic maneuverability to enable targeted navigation. The microrobots' fluorescence switching mechanism is elucidated through comprehensive spectroscopy, microscopy, and X-ray diffraction analyses, revealing molecular-level structural transformations upon interaction with gastric acid and antacids. These transformations, specifically protonation and deprotonation of the microrobots' fluorescent components, prompt a distinct fluorescence response correlating with pH shifts. In vitro and ex vivo experiments, simulating stomach conditions, confirm the microrobots' efficacy in pH-responsive imaging. The results showcase the promising diagnostic potential of microrobots for gastrointestinal tract diseases, marking a significant advancement in imaging-based medical diagnostics at targeted locations.

1. Introduction

Gastric acid, primarily composed of hydrochloric acid, pepsin, and lipase, plays a vital role in food digestion by breaking down proteins into several polypeptides and amino acids.[1] pH of gastric acid in the range of 1.5–3 is critical for a healthy digestive system and provides significant protection from microorganisms and pathogenic infections introduced through ingested food.[2,3] Imbalances in gastric acid secretion lead to various gastrointestinal disorders, including gastroesophageal reflux disease (GERD) and peptic ulcers. Proton pump inhibitors (PPIs) and antacids are the most commonly used medications for acid reflux treatment to control acid secretion and their acidity, respectively.[4] To assess the efficacy of these medications toward gastric disorders, monitoring intragastric acidity is highly critical.[5,6] Although traditional techniques, such as esophageal pH testing and the Heidelberg capsule method, offer insightful information about the pH changes of the gastric acid, most of these methods are insensitive and invasive, lacking real-time

N. Senthilnathan, C. M. Oral, M. Pumera
Future Energy and Innovation Laboratory
Central European Institute of Technology
Brno University of Technology
Purkyňova 123, Brno 61200, Czech Republic
E-mail: martin.pumera@ceitec.vutbr.cz

A. Novobilsky
Department of Pharmacology and Toxicology
Veterinary Research Institute
Hudcova 296/70, Brno 62100, Czech Republic

The ORCID identification number(s) for the author(s) of this article can be found under https://doi.org/10.1002/adfm.202401463

DOI: 10.1002/adfm.202401463

M. Pumera
Advanced Nanorobots & Multiscale Robotics Laboratory
Faculty of Electrical Engineering and Computer Science
VSB – Technical University of Ostrava
17. listopadu 2172/15, Ostrava 70800, Czech Republic

M. Pumera
Department of Medical Research
China Medical University Hospital
China Medical University
No. 91 Hsueh-Shih Road, Taichung 40402, Taiwan

M. Pumera
Department of Chemical and Biomolecular Engineering
Yonsei University
50 Yonsei-ro, Seodaemun-gu, Seoul 03722, South Korea

monitoring capabilities and causing discomfort for the patient.[7,8]

pH-responsive fluorescent molecular materials, polymers, quantum dots, and nanoparticles with high sensitivity have been widely used in bio-related applications, including controlled drug delivery, therapeutic applications, and pH sensing within cells, organelles, tissues, and living animals.[9–12] Fluorescent molecular materials stand out among the other materials due to their structural and fluorescence tailorability, and they are further appealing due to their excellent thermal-, chemical-, and photostability. However, it is worth noting that most fluorescent molecular materials suffer from weak solid-state fluorescence, a phenomenon known as "aggregation-caused quenching" (ACQ), and lack of target selectivity, limiting their feasibility in sensing applications.[13] Instead of focusing solely on designing molecular materials with high target selectivity for bio-sensing applications, an alternative and effective strategy has been adopted in this study to devise molecular materials-based microrobots with remotely controlled navigation features in response to external stimuli. This approach not only simplifies the design process but also proves to be highly effective for targeted sensing of physiological changes within the bio-system.[14]

The utilization of micro/nanorobots in the biomedical field is constantly advancing[15–18] as they possess significant potential in the medical sector to replace conventional tethered robotic systems. The ability of microrobots to navigate in hard-to-operate areas of the body highlights their prominence as untethered small-scale surgical instruments toward non-invasive diagnosis and therapy.[19–21] Among the microrobots that can exhibit locomotion under different stimuli, such as light irradiation,[22–24] magnetic field,[25–27] electric field,[28,29] and acoustic waves,[30–32] magnetically driven microrobots are prominent candidates for bio-related applications because of their precisely controllable fuel-free navigation features, even in high penetration depths, without damaging the tissue.[33–35] Our research group has successfully developed such microrobots for various biomedical and environmental remediation applications, including biofilm eradication, prostate cancer therapy, and the removal of pollutants from water (micro/nanoplastics, nitroaromatic explosives, and organic toxic pollutants).[36–41] Although magnetic microrobots are promising candidates for these applications, the requirement of tracking can be considered a significant challenge. In this regard, fluorescence emission is a highly sensitive and powerful tool that can play a pivotal role in both tracking and sensing applications within biological systems. Its significance lies in their non-invasive measurement possibility without disturbing the physiological functions of living systems. Previously, our research group has crafted fluorescent microrobots for organic dye degradation and metal ion detection applications.[42,43] Fluorescent microrobots have widespread use in diverse biomedical applications, such as imaging-guided drug delivery and related therapeutic interventions.[44–47] For instance, a few studies involving zinc- and magnesium-based fuel-free microrobots have been reported for gastric acid neutralization therapy in the gastrointestinal (GI) tract.[48–50] Recently, metal-based micromotors coated with commercially existing NIR-II fluorescent dyes have been reported as proton-responsive fluorescent probes specifically designed for GI imaging.[51] Here, we designed a new set of multi-fluorescent molecular materials-based microrobots to monitor gastric acid pH changes. To the best of our knowledge, for monitoring the acidity of intragastric acid, fluorescent molecular material-based microrobots have not been reported previously. Our choice of using diaminodicyanoquinodimethanes (DADQs) is noteworthy due to their pH-dependent fluorescence switching properties[52,53] and strong solid-state fluorescence emission, popularly known as "aggregation-induced emission (AIE)".[54] Furthermore, DADQ derivatives have been reported as biomarkers for the bacterial spores and stomatal cells of plants, highlighting their suitability for bio-related applications.[55,56]

In the present study, 7,7-bis(2-(2-aminoethyl)pyridino)−8,8-dicyanoquinodimethane (BAP) molecules with blue (BAP-B), green (BAP-G), and orange (BAP-O) fluorescence are synthesized for the fabrication of Fe_3O_4-decorated multi-fluorescent magnetic microrobots. In this microrobot design, fluorescent BAP molecules are the primary building block of the microrobots, and Fe_3O_4 nanoparticles are incorporated to magnetize the microrobots to facilitate motion, navigation, and collectability. In addition, spectroscopic and microscopic analyses provide insight into the molecular changes associated with the microrobots' fluorescence switching. As illustrated in **Scheme 1**, fluorescence imaging studies successfully demonstrate the cyclic pH variations of gastric acid by monitoring the fluorescence changes of the fluorescent microrobots at different pH conditions. Such signaling can pave the way for the utilization of fluorescent microrobots to diagnose GI tract infections. The fluorescent microrobots recognize the pH fluctuations and can also "recall" the acidic pH they passed through —even if they return to the neutral pH solution— by radiating distinct colors for a specific duration (Scheme 1c). Since memory is one of the key elements of intelligence, we introduce mobile intelligent microrobots in this study.

2. Results and Discussion

2.1. Fabrication and Characterization

Polymorphs of BAP molecules with different fluorescence were synthesized by adopting different synthetic conditions. BAP-B was synthesized by the direct addition of 2-(2-aminoethyl)pyridine into the acetonitrile solution of tetracyanoquinodimethane (TCNQ) at 72 °C for 3 h (**Figure 1a**).[52] Conversely, BAP-G was synthesized in tetrahydrofuran (THF) from the same reactants at 66 °C for 3 h. ^{1}H NMR spectra of both BAP-B and BAP-G served as an evidence for their structural integrity and purity (Figure S1, Supporting Information). The molecular structure and unit cell molecular assembly of BAP-B and BAP-G crystals were determined using single-crystal X-ray diffraction analysis (Figure 1b–e). Single-crystal X-ray diffraction analysis further reveals that BAP-B and BAP-G molecules exhibit characteristic average dihedral angles of 46.11° and 42.35°, respectively, between the benzenoid core ring and diaminomethylene of BAP moiety (Tables S1, S2, Supporting Information). BAP-B crystallizes as a $P2_12_12_1$ space group in its acetonitrile solution,[52] whereas BAP-G crystallizes as a $P2_1/c$ space group in the DMSO–water solvent mixture. The H-bonding interlinked supramolecular assembly of BAP-B and BAP-G molecules in the crystals is depicted in Figures S2 and S3 (Supporting Information). On the other hand, BAP-O was prepared by treating pure BAP-G crystals with trifluoroacetic

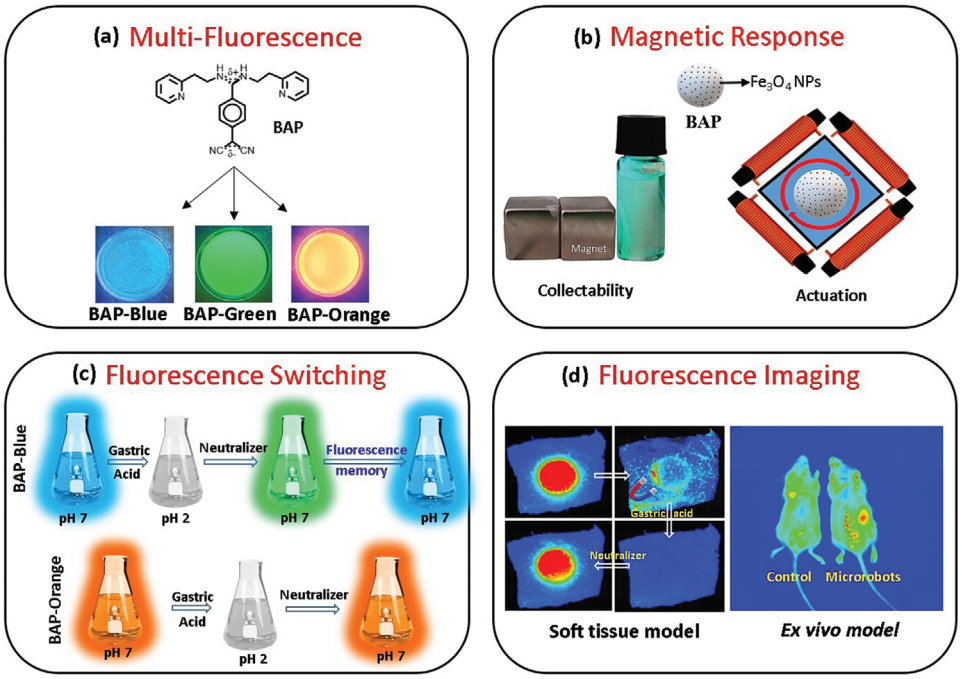

Scheme 1. Schematic representation of the multi-fluorescent magnetic microrobots for monitoring cyclic pH variations in gastric acid. a) Multi-fluorescent BAP (7,7-bis(2-(2-aminoethyl)pyridino)−8,8-dicyanoquinodimethane)-based microrobots. b) Magnetic collectability and actuation of the microrobots under external magnetic fields. c) Fluorescence switching of BAP microrobots at different pH. d) Fluorescence imaging of BAP-O microrobots at different pH in soft tissue sandwich model and ex vivo fluorescence imaging of mice before (control) and after injecting BAP-O microrobots.

acid for an extended duration,[57] as outlined in the Materials and Methods section (structural features are shown in Figure S4a, Supporting Information). The ^{1}H NMR spectrum of crude BAP-O reveals the retention of characteristic peaks observed in BAP-G with a downfield shift, along with the emergence of new proton signals originating from attachments to the dicyanomethylene carbon (δ = 5.30 ppm) and pyridine groups (δ = 4.15 ppm) as illustrated in Figure S4b (Supporting Information). The ^{19}F NMR spectrum proves the presence of trifluoroacetic acid moiety in the crude BAP-O (Figure S4c, Supporting Information). The results demonstrate that BAP-O is the protonated form of BAP-G, and post-purification, its peak positions are consistent with those of pure BAP-G (Figure S5, Supporting Information).

Electronic absorption and emission spectra of all BAP molecules are shown in Figure 1f,g, respectively. In the solid state, BAP-B, BAP-G, and BAP-O molecules exhibit absorption maxima at 360, 385, and 385 nm with a shoulder peak at 522 nm, respectively, while in acetonitrile solution, all molecules absorb the maximum at around 385 nm. The observed significant blueshift in the solid absorption spectrum of BAP-B can be attributed to the push–pull molecular environment. This shift results from the antiparallel orientation of neighboring molecular dipoles, creating a localized electric field that elevates the excited energy levels, consequently increasing the S^0-S^1 energy gap.[52,54] The emission maxima of BAP-B, BAP-G, and BAP-O molecules in the solution state are observed at 477, 480, and 583 nm, respectively. In contrast, in the solid state, their maximum emissions occur at 447, 493, and 583 nm, respectively. In addition to the blueshift observed in the solid-state emission spectra, there is a remarkable enhancement in the intensity of solid-state emissions to that of solution-state emission at an equivalent optical density. The fluorescence enhancements are likely due to the hindrance of intramolecular and intermolecular non-radiative excited state energy decay. The fluorophores with strong solid-state fluorescence emission are promising candidates for bio-related applications, and this enhancement phenomenon is well-known as "aggregation-induced emission" (AIE).[58] The fluorescence emission of BAP-G in the solvent mixture of water and THF exhibits significant enhancement when the water fraction is increased from 0% to 95%, as depicted in Figure S6 (Supporting Information), highlighting its aggregation-induced emissive property.

BAP-B, BAP-G, and BAP-O microparticles having decoration of Fe_3O_4 nanoparticles were fabricated using a simple reprecipitation method, as shown in Figure S7a (Supporting Information). Fe_3O_4 nanoparticles are employed to magnetize the microparticles and thereby facilitate their motion in the presence of a magnetic field, and thus called as microrobots. According to field emission scanning electron microscopy (FESEM) images (**Figure 2a**), BAP-B, BAP-G, and BAP-O microparticles have similar morphologies after incorporating Fe_3O_4 nanoparticles, as depicted in Figures S7b–m (Supporting Information), and the size of the microrobots is found to be in the range of 500 nm to 6 µm. Energy-dispersive X-ray spectroscopy (EDX) mapping confirms the successful attachment of Fe_3O_4 nanoparticles on the surface of the carbon-based microrobots during the fabrication process. This attachment is evident from the presence of iron and oxygen elements, as illustrated in Figure 2b. Space group variations between BAP-B and BAP-G molecules are likely to induce distinct molecular self-assembly processes and particle growth

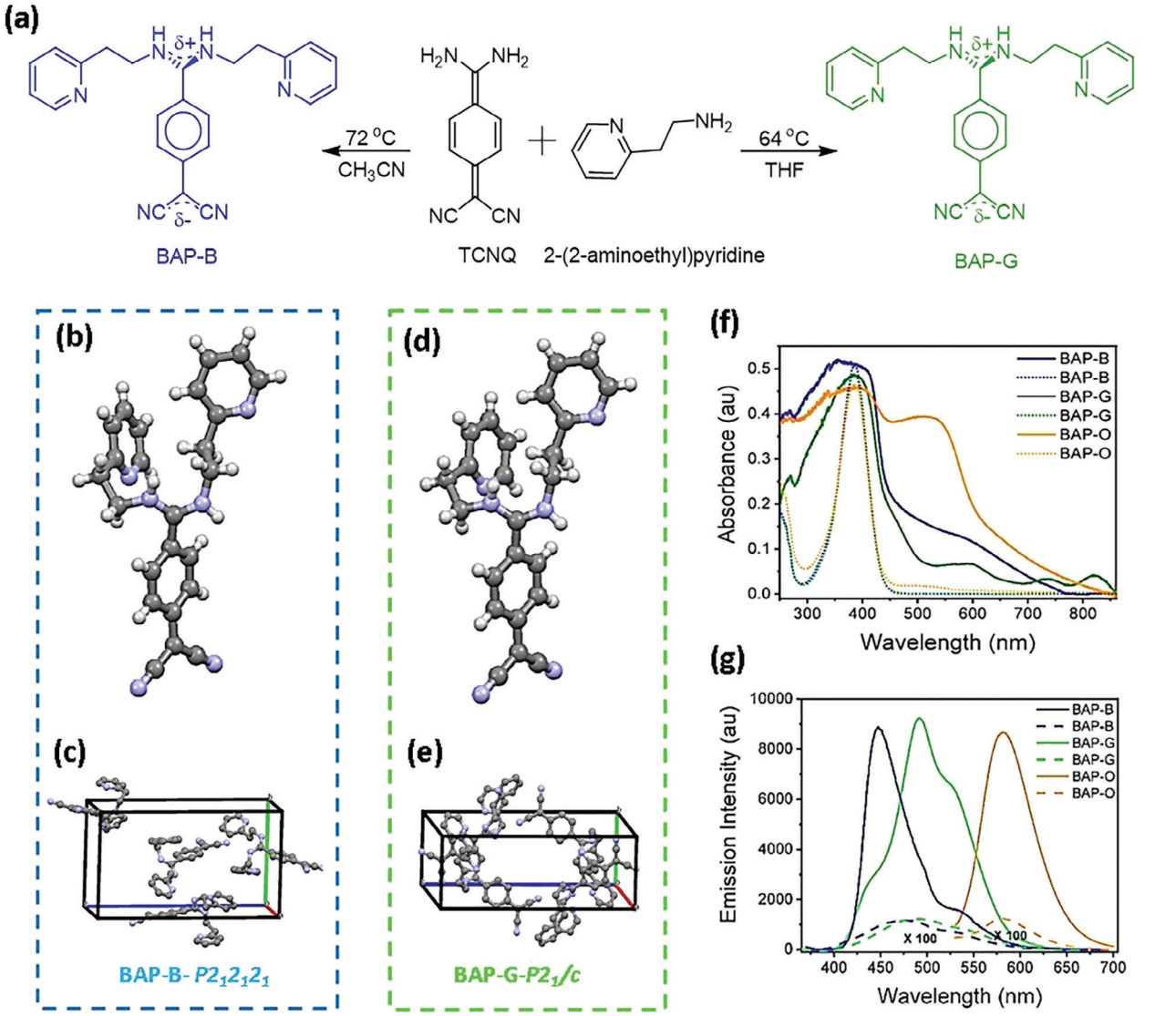

Figure 1. Synthesis and characterization of 7,7-bis(2-(2-aminoethyl)pyridino)−8,8-dicyanoquinodimethane (BAP). a) Schematic representation for the synthesis of BAP-B and BAP-G. b,d) Molecular structure and c,e) unit cell molecular assembly of b,c) BAP-B, and d,e) BAP-G determined using single-crystal X-ray diffraction analysis, where C: grey, N: blue, and H: light gray. f) Absorption and g) emission spectra of BAP-B (Ex: 350 nm), BAP-G (Ex: 350 nm), and BAP-O (Ex: 520 nm) in solid- (continuous lines) and solution-state (dotted lines). Solution-state emission spectra of BAP molecules were multiplied by a factor of 100 to improve their visibility.

mechanisms, leading to the formation of particles with diverse morphologies and surface roughness. These characteristics play a crucial role in varying degrees of attachment of Fe_3O_4 nanoparticles on the surfaces of both BAP-B and BAP-G microparticles, as shown in Figures 2a and S7 (Supporting Information). Notably, the protonated state of BAP-O microrobots exhibits enhanced attraction towards Fe_3O_4 nanoparticles, as depicted in Figure 2a, thanks to the ionic interactions. Fluorescence microscopic images in Figure 2c demonstrate the multi-fluorescent emissive features of microrobots, and it is important to highlight that the observed fluorescence colors of the microrobots are consistent with their emission spectra. The impact of the fabrication process on the molecular structures of BAP molecules in the structure of microrobots was analyzed using Fourier-transform infrared (FTIR) and powder X-ray diffraction (PXRD) studies (Figures 2d–g and S8 (Supporting Information)). PXRD patterns of as-prepared BAP-B, BAP-G, and BAP-O, as well as the corresponding microrobots, indicate that all these samples exhibit a crystalline nature. The simulated X-ray diffraction patterns of BAP-B and BAP-G are closely matched with those of their as-prepared samples and microrobots. Additionally, in the FTIR spectra, characteristic peaks, and peak positions of as-prepared BAP-B and BAP-G remain unchanged for the microrobots, suggesting the absence of structural modifications during the fabrication process. However, in the preparation of BAP-O, new peaks emerged at 1677, 1632, and 1198 cm^{-1}, along

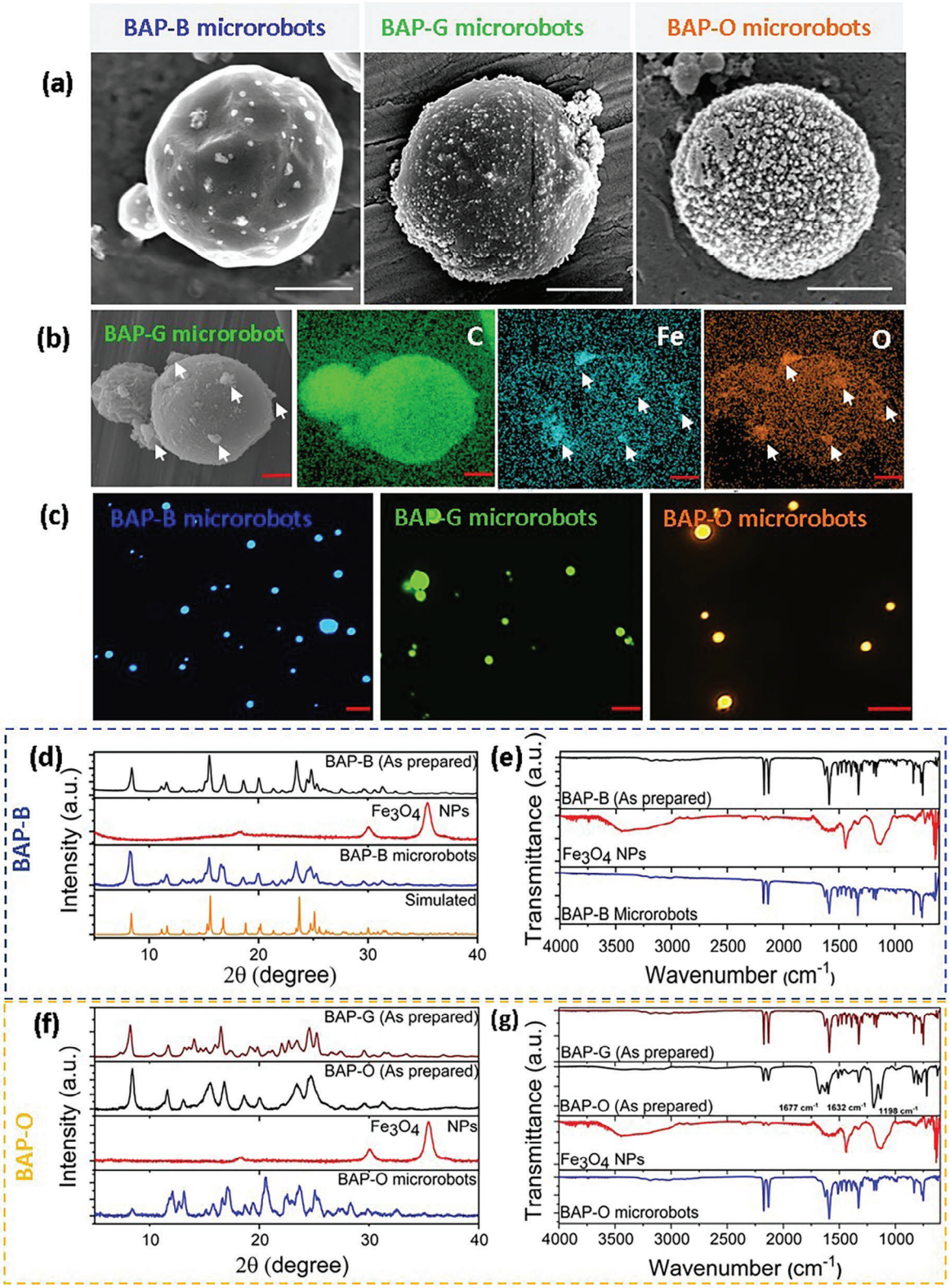

Figure 2. Characterization of BAP microrobots. a) FESEM images of the BAP-B, BAP-G, and BAP-O microrobots (Scale bars: 1 µm). b) EDAX analysis of an individual BAP-G microrobot decorated with Fe_3O_4 nanoparticles, showing the presence of carbon, iron, and oxygen elements (Scale bars: 2 µm). c) Fluorescent microscopy images of BAP-B, BAP-G, and BAP-O microrobots (Scale bars: 5 µm). d,f) PXRD and e,g) FTIR spectra of as-prepared microcrystals and microrobots of d,e) BAP-B and f,g) BAP-O. A simulated XRD pattern of BAB-B is also shown for reference.

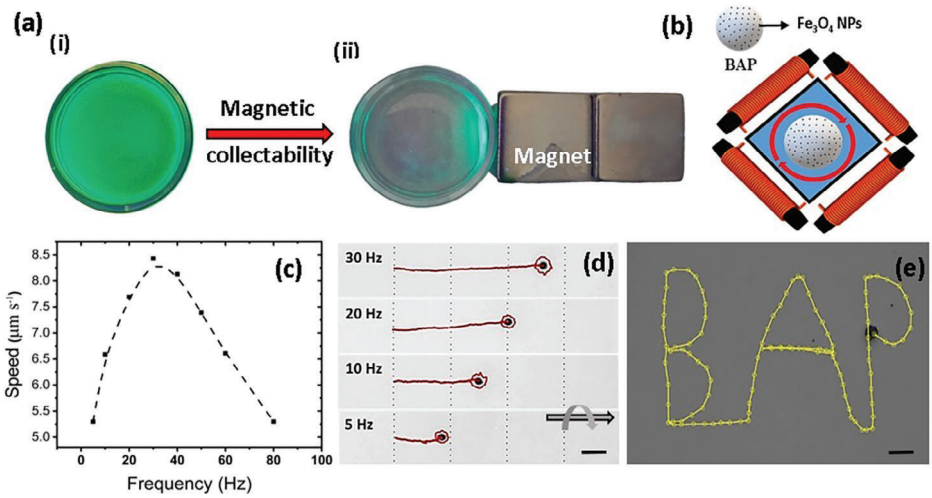

Figure 3. Collectability and actuation of microrobots under external magnetic fields. a) Photographs of aqueous dispersions of BAP-G microrobots under UV light (i) before and (ii) after the magnetic collection. b) Pictorial representation of the custom-built magnetic setup used for motion experiments. c) Average speed and d) displacement of BAP-G microrobots at different frequencies under a magnetic field of 5 mT (Scale bar: 20 μm). e) Magnetically controlled navigation of a BAP-G microrobot on the predesigned "BAP track" (Scale bar: 20 μm).

with characteristic peaks of as-prepared BAP-G. The peaks of BAP-O at 1677 and 1198 cm^{-1} are attributed to the protonation of pyridine and the presence of C—F bond functionalities (from the trifluoroacetic acid), respectively. The emergence of new peaks proves once again that BAP-O is the protonated form of BAP-G. Notably, the characteristic peaks of Fe_3O_4 nanoparticles are not observed in the spectra of any BAP microrobots due to their limited presence compared to BAP molecules.

2.2. Magnetic Actuation

The magnetic properties of the as-prepared BAP-G and the corresponding microrobots were assessed through vibrating sample magnetometer (VSM) analysis, and the resulting magnetic hysteresis loops are reported in Figure S9 (Supporting Information). The results reveal that bare BAP-G microparticles have a negligible magnetic response, while the magnetic properties significantly change for BAP-G microrobots due to the presence of Superparamagnetic Fe_3O_4 nanoparticles. Additionally, the magnetic collectability of the microrobots was tested using a neodymium–iron–boron (NdFeB) magnet close to BAP microrobots, as shown in **Figure 3**a, and the images were captured under the illumination of UV light. In Figure 3a(i), the dispersion of microrobots in an aqueous medium is depicted, while Figure 3a(ii) illustrates the microrobots being attracted toward the magnet. Microrobots that exhibit motion with localization capability within animal bodies under the influence of a magnetic field highlight significant promise for imaging applications in living organisms.[59] Therefore, magnetically induced locomotion of the BAP-G and BAP-O microrobots (Movies S1 and S2, respectively (Supporting Information)) and their controlled navigation (Movie S3, Supporting Information) were thoroughly analyzed using a customized magnetic setup equipped with an optical microscope and a sophisticated controlling unit. In this setup, three orthogonal coil pairs were employed to generate a transversal rotating magnetic field to induce the motion of microrobots (Figure 3b). To determine the step-out frequency of the microrobots, average speed values were calculated in the range of 10–80 Hz while keeping the magnetic field as 5 mT along the x-axis (Figure 3c). The step-out frequency of BAP-G microrobots is identified as 30 Hz at 5 mT, as depicted in Figure 3c,d. At 30 Hz, the microrobots achieved their maximum speed of 8 μm s^{-1}, and average speed values decreased beyond this frequency. The decrease in speed values is attributed to the loss of microrobots' synchronization with the higher magnetic frequency, which is a result of the increased viscous torque exerted by the surrounding liquid.[60,61] Although there are varying levels of Fe_3O_4 nanoparticle attachment observed on BAP-B and BAP-G microrobots as shown in Figures 2a and S7 (Supporting Information), their speed remains relatively same at around 8 μm s^{-1}. In contrast, the higher concentration of Fe_3O_4 nanoparticles adhered to the surface of BAP-O microrobots resulted in an enhanced actuation speed of approximately 10 μm s^{-1}, surpassing that of both BAP-B and BAP-G microrobots. Apart from speed, controlled navigation is also a critical feature of microrobots for their bio-related applications and it is appraised by observing their movement upon changing the direction of the magnetic field using a controller. Figure 3e and Movie S3 (Supporting Information) illustrate that a single microrobot can be navigated along a predefined "BAP track" by only adjusting the direction of the external magnetic field (5 mT, 20 Hz). The fast response and the remotely controllable navigation of magnetic BAP microrobots make them a promising candidate for various bio-medical applications, such as targeted diagnosis, monitoring, and nanosurgery.

2.3. Fluorescence Properties

The pH-dependent optical characteristics of BAP-B, BAP-G, and BAP-O microrobots were comprehensively investigated under various conditions. Electronic absorption and fluorescence

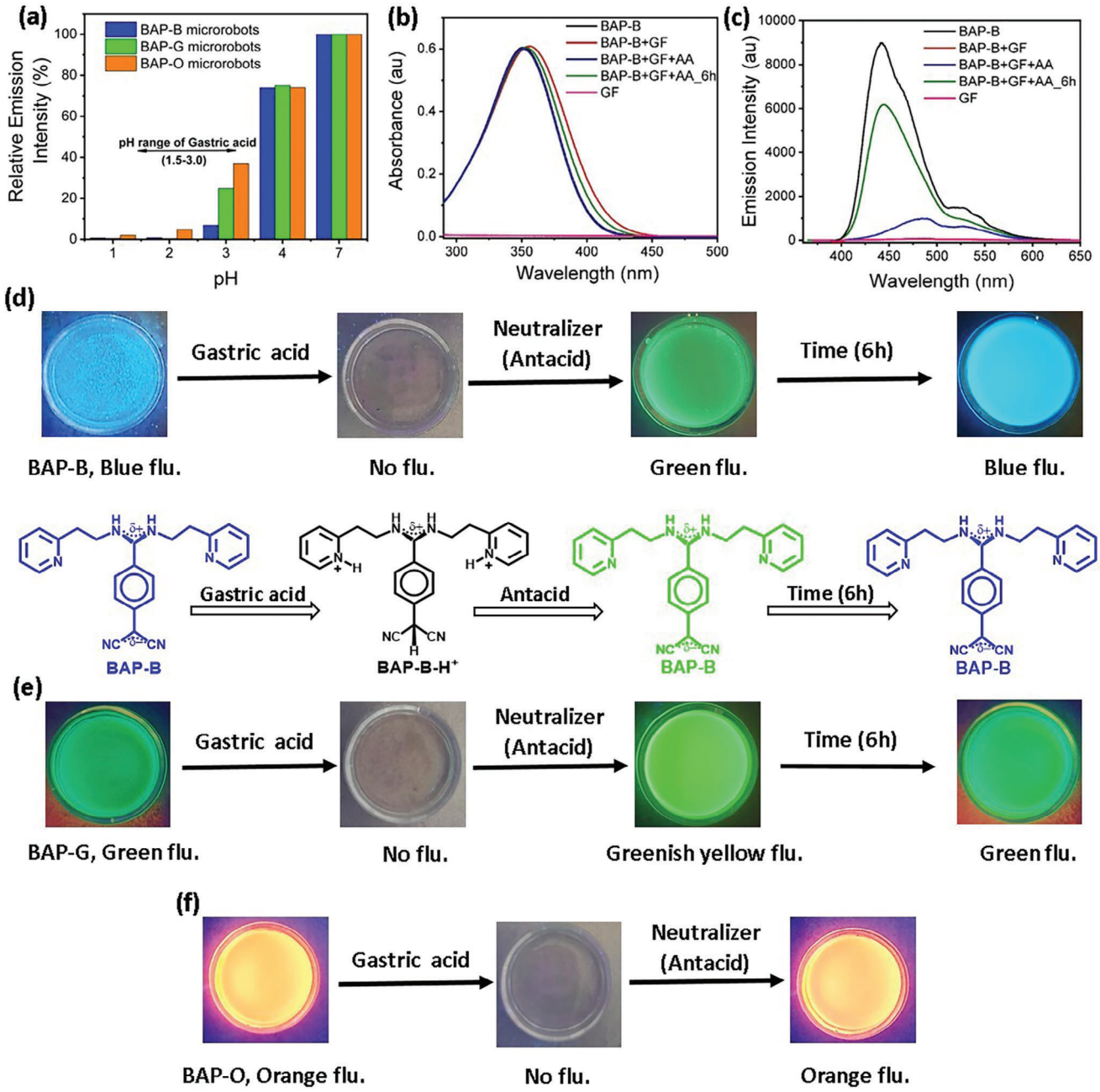

Figure 4. pH-dependent fluorescence switching of microrobots and the memory effect. a) Variation of the fluorescence intensity of BAP-B, BAP-G, and BAP-O microrobots at different pH. b) Absorption and c) emission spectra (Ex: 350 nm) of BAP-B microrobots in water and gastric fluid (GF), followed by the addition of antacid. Photographs of d) BAP-B, e) BAP-G, and f) BAP-O microrobots at different pH conditions: initially in their original state in water (pH 7) and then after the addition of gastric fluid (GF, pH 2), and finally following the subsequent addition of antacid (AA, pH 7). A plausible mechanism of BAP-B's protonation and deprotonation after the addition of gastric acid and antacid is provided below the image (d). All the photographs are taken under UV light (365 nm) illumination.

emission spectra of the aqueous dispersion of all BAP microrobots were recorded at different pH, as depicted in Figure S10 (Supporting Information), and the results are summarized in **Figure** 4a. The results indicate that the fluorescence emission intensity of all BAP microrobots in the aqueous dispersions/solutions decreases as the acidity of the solution increases. In other words, the fluorescent BAP microrobots and their fluorescence emission are stable in the pH range of 4–7, and the fluorescence emission intensity experiences a significant fall when the pH drops below 3 due to their significant dissolution. These initial findings offer promising prospects for monitoring pH changes of gastric acid (pH 1–3) by employing the fluorescent BAP microrobots. In the process of monitoring pH changes of gastric acid, the following series of experiments were conducted.

Initially, BAP-B microrobots were subjected to gastric acid and subsequently treated with an antacid (neutralizer), as shown in Figure 4d–f, to understand their fluorescence switching properties. Blue fluorescent (BAP-B) microrobots lose their fluorescence when treated with gastric acid due to their dissolution; the lost fluorescence is immediately regained after adding an antacid due to the reformation of BAP microparticles (Figure 4d). During the dissolution process in gastric acid, BAP particles in the microrobots are dissolved, and then decorated Fe_3O_4 nanoparticles are detached from the structure of the microrobots. Most of the nanoparticles are not reattached to the surface of BAP microparticles during the reformation process after the addition of antacid. Interestingly, the regained fluorescence emission appears green, but over several hours, it gradually returns to its original blue fluorescence. This transition is one of the exciting features observed in the process of monitoring pH changes in gastric acid, which was named as "fluorescence memory." Similar experiments were also carried out with BAP-G and BAP-O microrobots, and the results are summarized in Figure 4e,f. In the case of BAP-G microrobots, lost fluorescence following exposure to gastric acid is rapidly restored to a greenish-yellow fluorescence upon the addition of an antacid. Subsequently, it is transformed back to its original green fluorescence after several hours (Figure 4e). The underlying reasons for these transitions were elucidated using FTIR and PXRD analyses and discussed later. On the contrary, the "fluorescence memory" was not observed in BAP-O microrobots, and its original fluorescence was regained

Immediately after the addition of an antacid (Figure 4f). This difference in the behavior of BAP-O microrobots from BAP-B and BAP-G microrobots is likely attributed to the structural modifications undergone by BAP-O during its exposure to trifluoroacetic acid. It is important to note that BAP-B and BAP-G were synthesized from the same reactants under different conditions, whereas BAP-O is the protonated form of BAP-G as depicted in Figure S4 (Supporting Information).

The fluorescence switching of the microrobots in response to pH changes is also validated through spectroscopic analysis. The electronic absorption and fluorescence emission spectra of bare microrobots in water, gastric acid, and following the addition of an antacid are depicted in Figures 4b,c. Figure 4b illustrates that BAP-B microrobots consistently display an absorption maxima at 355 nm in all the cases. Even though BAP-B microrobots have similar optical densities (highlighting the same concentration) in all the cases, they exhibit different fluorescence emission with intensity variations, as shown in Figure 4c, due to the molecular structural changes that occur in the BAP-B moiety upon the addition of gastric acid and antacid. Initially, the aqueous dispersion of BAP-B microrobots exhibits an emission maximum at 444 nm, consistent with that of the microcrystalline solid form. However, upon the addition of gastric acid, the fluorescence peak almost disappears due to the protonation of BAP-B. The subsequent addition of antacid, specifically sodium bicarbonate, restores them to their deprotonated state, thereby bringing back the fluorescence peak at 485 nm with a notable red-shift of 40 nm. The red-shifted fluorescence peak gradually returns to its original position at 444 nm over time. In simpler terms, a faint green fluorescence peak transforms into a vivid blue fluorescence peak within a span of 6 hours, and this transition was previously referred to as "fluorescence memory" transition. A similar experiment was repeated with BAP-G and BAP-O microrobots, yielding similar outcomes for BAP-G but not for BAP-O. The absorption and fluorescence emission maxima of the aqueous dispersion of BAP-G microrobots are observed at 355 and 492 nm, respectively, consistent with that of their microcrystalline. The fluorescence peak of BAP-G disappears upon the addition of gastric acid, and it is restored after the introduction of the antacid. Notably, the fluorescence memory transition is not significantly observed in the case of BAP-G and not observed at all for BAP-O. As shown in Figure S11 (Supporting Information), fluorescence emission peaks of BAP-O before and after the addition of gastric acid/antacid is not switched significantly. The lack of a noticeable change indicates the absence of a fluorescence memory transition for BAP-O microrobots.

To gain deeper insights into molecular-level changes underlying the fluorescence memory transition of BAP microrobots, FTIR and PXRD analyses were carried out (Figures S12–S14, Supporting Information). In the FTIR analysis, remarkably, no changes were visible in the vibrational frequencies of key functional moieties of all BAP microrobots, even after the addition of gastric acid/antacid, as shown in Figures S12–S14a (Supporting Information). The absence of molecular structural changes suggests that the fluorescence memory transition may occur due to some other factors. In order to reveal it, PXRD analysis was carried out (Figure S12–S14b, Supporting Information). The PXRD analysis unveils that the reversible crystal-amorphous transition that occurs in BAP microrobots leads to their fluorescence memory transitions. The diffraction patterns clearly reveal the initial crystalline nature of as-prepared BAP-B, BAP-G, and BAP-O, as well as the corresponding microrobots. As illustrated in the diffraction patterns, except for BAP-O microrobots, the other two microrobots lose their crystallinity upon the addition of gastric acid and antacid, which explains the absence of a fluorescence memory transition for BAP-O microrobots. Intriguingly, they gradually re-establish their crystallinity within a 6-hour period.

2.4. Fluorescence Imaging

The process of practical implementation of monitoring pH fluctuations in gastric acid using BAP fluorescent microrobots was initiated with a comprehensive in vitro imaging analysis. In these experiments, equal quantities of bare BAP-B, BAP-G, and BAP-O microrobots were individually placed in well plates containing water, gastric acid, and a mixture of gastric acid and antacid, as illustrated in **Figure 5**a, and fluorescence imaging was conducted using appropriate excitation and emission wavelengths. As shown in Figure 5a, BAP microrobots display strong fluorescence in the wells containing water or a mixture of gastric acid and antacid. However, they exhibit no fluorescence emission in the gastric acid wells. These results suggest that all BAP microrobots possess the capability to measure intragastric acidity, making them suitable for a diverse range of in vitro investigations. Furthermore, a soft tissue model (Figure 5b) was also utilized to investigate the imaging performance of microrobots when they are present below a tissue. For these experiments, aqueous suspensions of BAP-B, BAP-G, and BAP-O microrobots were separately injected into the tissue sandwich model filled with 0.5 mL

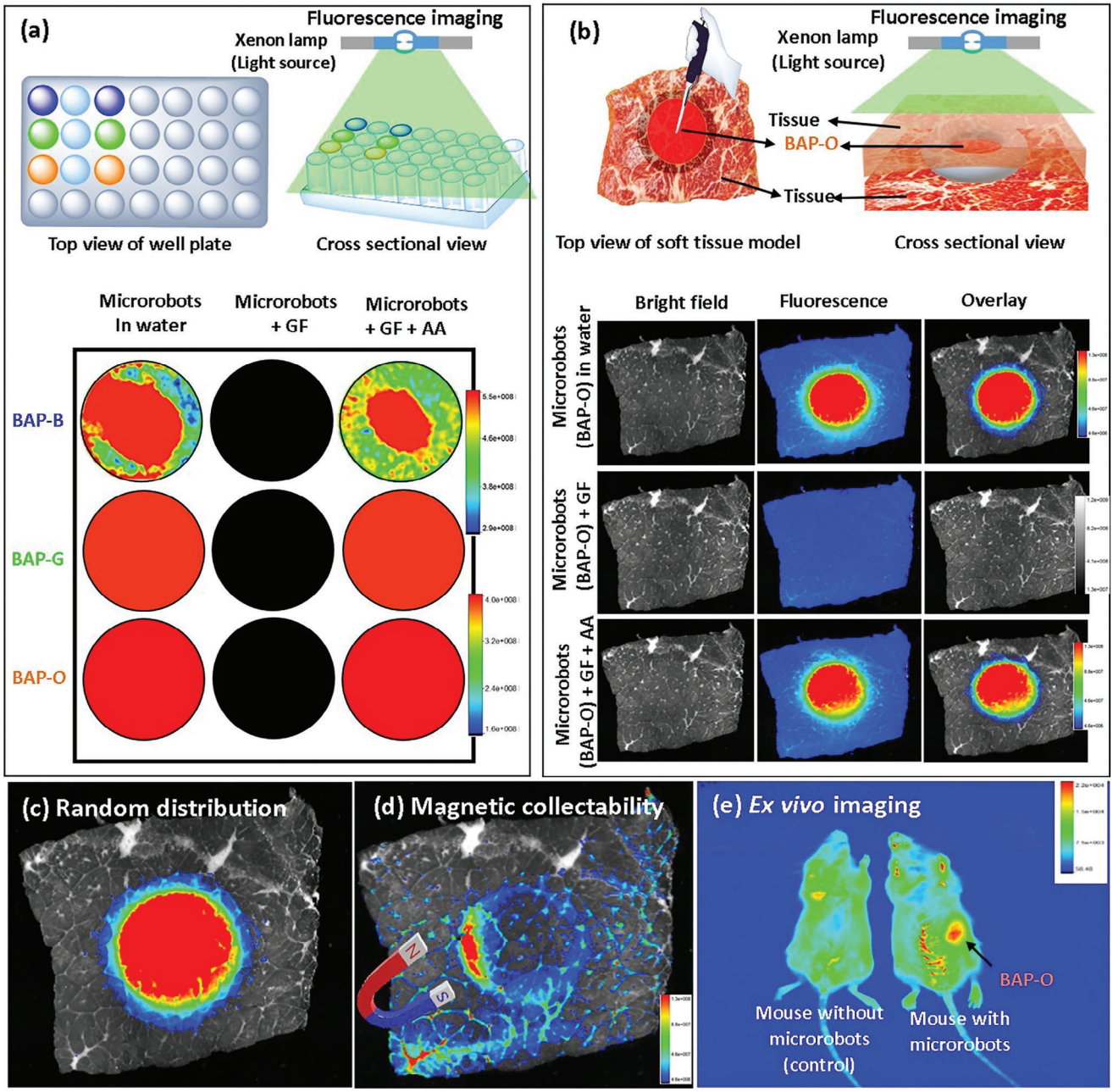

Figure 5. Fluorescence imaging. a) Schematic description and fluorescence images of BAP-B, BAP-G, and BAP-O microrobots in water, in gastric fluid (GF), and in a mixture of GF and antacid (AA). b) Schematic description of a soft tissue model utilized during imaging experiments and fluorescence response of BAP-O microrobots in water, in GF, and followed by the addition of AA into the tissue model. c,d) Random distribution and magnetic collectability of BAP-O microrobots in the tissue model. e) Ex vivo fluorescence imaging of mouse before (left) and after (right) injection of BAP-O microrobots (injection location is shown with an arrow). Ex: 410 nm and Em: 535 nm for BAP-B and BAP-G microrobots. Ex: 410 nm and Em: 600 nm for BAP-O microrobots.

of water, and then imaged under the suitable excitation wavelengths. As an important observation, the fluorescence emitted by BAP-B and BAP-G microrobots was not detectable in the tissue model (Figure S15, Supporting Information). This lack of detection is attributed to the interference and overlap with the autofluorescence of the tissues utilized for the experiments. However, in contrast to BAP-B and BAP-G microrobots, BAP-O microrobots were successfully able to emit detectable fluorescence in the tissue model (Figure 5b). This difference could be a result of the emission range of BAP-O microrobots rather than the autofluorescence of the tissue, enabling their distinct identification and monitoring capabilities in a complex environment.[62] Later, an aqueous dispersion of BAP-O microrobots was injected into the tissue model filled with 0.5 mL of gastric acid (0.01 M), and

then an equal volume of antacid (0.01 M) was injected into the tissue model to mimic the fluorescence switching of BAP-O microrobots in acidic and neutral conditions of the human stomach, respectively, and then fluorescence imaging was performed. As consistent with the previous observations, BAP-O microrobots lose their fluorescence in acidic conditions and regain it in neutral pH conditions (Figure 5b).

Furthermore, the magnetic response of the microrobots was tested in a similar experimental condition. The mucus layer in the GI tract and stomach is a sticky and elastic gel that can effectively capture foreign particles, including drug molecules, on its surface.[63] In such a sticky environment, externally controlled navigation and magnetic collectability are crucial for microrobots to prevent adherence to the mucosal surface while en route to target location of the stomach. Because of the size of the magnetic setup, we could not successfully integrate it into the fluorescence imaging instrument. As a result, we could not display the benefit of microrobot motion in monitoring pH changes in gastric acid during ex vivo analysis. To overcome this issue, we employed a NdFeB magnet to generate a strong magnetic force to induce the collection of the microrobots to the place of interest. Figure 5c,d illustrate the successful magnetic collectability of the fluorescent BAP-O microrobots in the tissue sandwich model and prove their external controllability. We also examined the fluorescence emission of the BAP-O microrobots post-injection into the animal body to assess their suitability for in vivo imaging. For this experiment, a mouse without microrobots was used as a control. As seen in Figure 5e, the mouse without microrobots showed only autofluorescence signals, while the microrobots in the mouse could be monitored at the location of the injection. It's also worth noting that IC_{50} values for zwitterionic DADQ derivatives with hexylamine and piperazine functionalities[55,56] are reported to be more than 500 μg ml^{-1}. Consequently, it's reasonable to speculate that BAP microrobots are not likely to cause toxicity with their structural similarity to the derivatives reported as biocompatible in the literature. Overall, in vitro and ex vivo experiments emphasize the capability of BAP-O fluorescent microrobots to monitor pH variations in gastric acid, which can be utilized for diagnostics at targeted locations of the stomach.

3. Conclusion

In this study, we developed a series of multi-fluorescent molecular materials-based microrobots decorated with Fe_3O_4 nanoparticles via a simple reprecipitation method to monitor intragastric acidity. The motion analysis demonstrated the externally controllable navigation of microrobots in the presence of a magnetic field. Furthermore, we have demonstrated the fluorescence switching of the microrobots at different pH levels and their utilization in monitoring pH changes in gastric fluids through in vitro and ex vivo experiments. Microscopic and spectroscopic studies provided a deeper insight into the molecular structural changes associated with pH-sensitive fluorescence switching of BAP microrobots. To investigate the microrobots in a realistic scenario, a soft tissue-based human stomach simulation model was utilized. The imaging experiments highlighted a fast localization of BAP-O microrobots to the place of interest under the guidance of a magnetic field. Appreciable magnetic localization and ex vivo imaging performance of the microrobots emphasized their sensing capability toward real-time pH monitoring applications in targeted areas of the animal or human body. Therefore, this work revealed that these pH-responsive molecular-based microrobots hold great promise in imaging-assisted diagnostics of gastrointestinal disorders.

4. Experimental Section

Materials: 7,7,8,8-Tetracyanoquinodimethane (TCNQ, $C_{12}H_4N_4$, 98%), 2-(2-aminoethyl)pyridine ($C_7H_{10}N_2$, 95%), iron(II) sulfate heptahydrate ($FeSO_4{\cdot}7H_2O$, ≥99%), ferric chloride hexahydrate ($FeCl_3{\cdot}6H_2O$, ≥98%), calcium chloride dihydrate ($CaCl_2{\cdot}2H_2O$, ≥99%), trifluoroacetic acid (CF_3COOH, 99%), hydrochloric acid (HCl, 37%), sodium bicarbonate ($NaHCO_3$, 99.5%), sodium hydroxide (NaOH, ≥98%), and all solvents (HPLC grade) used in this work were purchased from Sigma Aldrich and utilized as received. Simulated gastric acid (without enzyme) was purchased from ProSense and used after dilution according to the manufacturer's instructions. Ultra-pure water was used for the fabrication of Fe_3O_4 nanoparticles and BAP microrobots.

Synthesis of BAP Molecules: BAP-B and BAP-G were synthesized by directly adding 149 mg of 2-(2-aminoethyl)pyridine into a 15 mL solution containing 100 mg of TCNQ at 70 °C for 3 hours. BAP-B was synthesized in acetonitrile solvent, while BAP-G was synthesized in THF solvent. The yellow solution of TCNQ turned into a dark-green solution after the addition of amines, and the resulting BAP precipitate was filtered after 3 hours and dried at room temperature. The resulting BAP-B and BAP-G precipitates were recrystallized using acetonitrile and a mixture of DMSO-water solvent systems, respectively. The yield of BAP-B and BAP-G was 85% and 80%, respectively. BAP-O was derived from BAP-G by treating it with trifluoroacetic acid at 140 °C for 15 minutes.

Preparation of Fe_3O_4 Nanoparticles: $CaCl_2{\cdot}2H_2O$ of 20 mg and 38 mg of $FeSO_4{\cdot}7H_2O$ were dissolved in 20 mL of water each and mixed for 5 mins at 25 °C. 37 mg of $FeCl_3{\cdot}6H_2O$ was added into this solution and stirred gently for 15 mins at 60 °C. Ammonium hydroxide solution (30%) was slowly added into the solution until reaching pH 11 and further stirred for 15 minutes. The resulting Fe_3O_4 nanoparticles were collected using a magnet, washed with ultra-pure water and ethanol several times, and dried at room temperature overnight.

Fabrication of Microrobots: BAP-B of 4 mg was dissolved in 2 mL of hydrochloric acid (0.1 M) containing 0.15 mg of Fe_3O_4 nanoparticles while sonication for 30 s. By introducing sodium hydroxide (1 M) solution into the acidic solution of BAP-B under sonication, the BAP-B molecules experienced immediate reprecipitation. During this process, the existing Fe_3O_4 nanoparticles in the acidic solution became trapped both inside and on the surface of the microrobots. Fe_3O_4 nanoparticles decorated BAP-B microrobots were collected using a magnet and dried at room temperature. The same procedure was also repeated to fabricate microrobots of BAP-G and BAP-O.

Spectroscopic Analysis: Electronic absorption and fluorescence emission spectra were recorded using a Jasco V-750 UV–vis spectrophotometer and a Jasco FP8300 spectrofluorometer, respectively. 0.1 mM acetonitrile solutions of BAP and their microcrystalline solids were used to record absorption and emission spectra. An equal quantity of BAP-B, BAP-G, and BAP-O microrobots was dispersed in the mixture of water, and HCl with different pH (1, 2, 3, 4, and 7), and their PL emission spectra were recorded. HCl was used to prepare solutions at different pH. A Metrohm 913 pH meter was used to measure the solution pH.

The quantity of BAP microrobots present in the dispersions/solutions was equalized by adjusting the optical density to the same value before recording emission spectra. Preparing the solutions/dispersions of BAP microrobots with the same optical density (representing equivalent BAP concentrations) to compare their fluorescence changes at varying pH was essential. This procedure ensures that the observed fluorescence changes in BAP microrobots were only from their pH-dependent fluorescence response and not from their concentration changes without any ambiguity.

FTIR spectra of the microrobots in a dry state were recorded using a Vertex 70v FTIR spectrometer equipped with a microscope Hyperion 3000.

Microscopic Analysis: The morphology of BAP microparticles and the corresponding microrobots was observed using a FEI Verios 460L SEM. Elemental analysis was conducted using a Tescan MIRA3 XMU SEM equipped with an EDAX detector. Samples for both SEM and EDAX analyses were prepared using a simple drop-casting method. A few drops of an aqueous dispersion of microrobots (1 mg/mL) were drop-cast on the copper-taped SEM stub, and 10 nm gold thin film was sputtered using a Leica EM ACE600 coater.

Magnetic Motion Analysis: Magnetic motion analysis of the microrobots was carried out in a custom-made magnetic setup consisting of three orthogonal coil pairs, all housed within a 3D-printed polylactic acid (PLA) backbone connected with a navigation controller. The motion of microrobots was captured using a Nikon Ts2R inverted microscope equipped with a Basler acA1920-155uc camera. In the experiments, the magnetic field of 5 mT was kept constant while the frequency was varied from 10 to 80 Hz. Sodium dodecyl sulfate (0.15%) was employed during the motion experiments. The speed and trajectory of the microrobots were analyzed from the captured videos using NIS-Elements Advanced Research software. At least 100 individual particles were tracked for each condition to calculate average speed values.

X-ray Diffraction Analysis: Single-crystal X-ray diffraction analysis of the single crystals of BAP-B and BAP-G were collected using Rigaku Oxford XtaLAB Synergy R custom diffractometer equipped with an automated crystal transport orientation and retrieval robot (ACTOR). A rotating-anode X-ray tube was employed to generate Cu K_α ($\lambda = 1.54$ Å) radiation and the data were collected at 120 K with a Hybrid Pixel Array Detector. The collected data were reduced using CrysAlisPro software (1.171.42.95a version). SHELXL-2019/3 software was utilized to solve and refine the crystal structure. Powder X-ray diffraction analysis was carried out using a Rigaku SmartLab 3 kW XRD diffractometer and data were collected using Cu K_α radiation at 40 kV and 30 mA. Simulated PXRD patterns of BAP-B and BAP-G were derived from their SCXRD data using Mercury 3.8 software.

Soft Tissue Model Preparation: A tissue sandwich model was prepared using soft tissue slices to mimic the human stomach. Two slices of soft muscle tissues (beef meat) with ≈0.5 mm thickness were sandwiched between each other, and all four corners were sealed using glue, as shown in Figure 5b. This model was referred as "tissue sandwich model".

Fluorescence Imaging: Gastric acid of 0.01 M and the same concentration of antacid were employed in the in vitro and ex vivo imaging experiments. Fluorescence imaging was conducted using a Bruker In-Vivo Xtreme II System equipped with a 400-watt Xenon lamp (350–1000 nm) and a highly sensitive CCD detector. Excitation (Ex) and emission (Em) filters were 410 and 535 nm for BAP-B and BAP-G microrobots, respectively. For BAP-O, the excitation filter was 410 and the emission filter was 600 nm. For ex vivo imaging, a dispersion of BAP-O microrobots (1 mg mL^{-1}) was subcutaneously injected into a mouse.

Supporting Information

Supporting Information is available from the Wiley Online Library or from the author.

Acknowledgements

N.S. acknowledges the financial support by the European Union's Horizon 2021 research and innovation program under the Marie Skłodowska-Curie grant agreement No. 101063710. N.S. thanks Dr. S. G. Ullattil for his contribution to SEM analysis. The authors would like to thank X. Peng and J. Jyoti for their help with VSM measurements. The work was supported by ERDF/ESF project TECHSCALE (No. CZ.02.01.01/00/22_008/0004587). This research was co-funded by the European Union under the REFRESH – Research Excellence for REgion Sustainability and High-tech Industries project number CZ.10.03.01/00/22_003/0000048 via the Operational Program Just Transition. A.N. was supported by the Project "FIT" (Pharmacology, Immunotherapy, nanotoxicology: CZ.02.1.01/0.0/0.0/15_003/0000495) from the Ministry of Education, Youth and Sports of the Czech Republic, and Ministry of Agriculture of the Czech Republic (MZE-RO0523). The authors acknowledge the CzechNanoLab research infrastructure supported by MEYS CR (LM2023051). The authors acknowledge CF Biomolecular Interactions and Crystallography of CIISB, Instruct-CZ Centre, supported by MEYS CR (LM2023042) and European Regional Development Fund-Project "UP CIISB" (No. CZ.02.1.01/0.0/0.0/18_046/0015974).

Open access publishing facilitated by Vysoke uceni technicke v Brne, as part of the Wiley - CzechELib agreement.

Conflict of Interest

The authors declare no conflict of interest.

Author Contributions

N.S. prepared and characterized the microrobots, interpreted the results, and wrote the manuscript draft. N.S. and C.M.O conducted motion experiments. C.M.O. collected fluorescence microscopy images and VSM data. A.N. collected in vitro and ex vivo fluorescence images. N.S. and M.P. originated the project idea. M.P. supervised the project. All authors contributed to the experimental design and manuscript preparation.

Data Availability Statement

The data that support the findings of this study are available from the corresponding author upon reasonable request.

Keywords

fluorescence sensing, gastric pH monitoring, magnetic microrobots, pH response

Received: January 24, 2024
Revised: April 24, 2024
Published online: May 17, 2024

[1] T. C. Martinsen, R. Fossmark, H. L. Waldum, *Int. J. Mol. Sci.* **2019**, *20*, 6031.
[2] S. A. Sarker, K. Gyr, *Gut* **1992**, *33*, 987.
[3] R. A. Giannella, S. A. Broitman, N. Zamcheck, *Gut* **1972**, *13*, 251.
[4] Y. Kinoshita, N. Ishimura, S. Ishihara, *J. Neurogastroenterol. Motil.* **2018**, *24*, 182.
[5] J. Wang, J. Li, Y. Li, Z. Zhang, L. Wang, D. Wang, L. Su, X. Zhang, B. Z. Tang, *Chem. Sci.* **2020**, *11*, 6472.
[6] Q. Ci, Y. Wang, B. Wu, E. Coy, J. J. Li, D. Jiang, P. Zhang, G. Wang, *Adv. Sci.* **2023**, *10*, 2206271.
[7] T. R. DeMeester, J. A. Wernly, C. I. Wang, C. A. Pellegrini, A. G. Little, P. Klementschitsch, G. Bermudez, L. F. Johnson, D. B. Skinner, *J. Thorac. Cardiovasc. Surg.* **1980**, *79*, 656.
[8] T. Ghosh, D. I. Lewis, A. T. R. Axon, S. M. Everett, *Aliment. Pharmacol. Ther.* **2011**, *33*, 768.
[9] Z. Fan, S. Zhou, C. Garcia, L. Fan, J. Zhou, *Nanoscale* **2017**, *9*, 4928.
[10] S. Li, K. Hu, W. Cao, Y. Sun, W. Sheng, F. Li, Y. Wu, X. J. Liang, *Nanoscale* **2014**, *6*, 13701.
[11] J. Li, C. Liu, Y. Hu, C. Ji, S. Li, M. Yin, *Theranostics* **2020**, *10*, 166.
[12] H. Ehtesabi, Z. Hallaji, S. Najafi Nobar, Z. Bagheri, *Microchim. Acta* **2020**, *187*, 150.

[13] Y. Huang, J. Xing, Q. Gong, L. C. Chen, G. Liu, C. Yao, Z. Wang, H. L. Zhang, Z. Chen, Q. Zhang, *Nat. Commun.* **2019**, *10*, 169.
[14] L. Cai, D. Xu, Z. Zhang, N. Li, Y. Zhao, *Research* **2023**, *6*, 44.
[15] G. T. van Moolenbroek, T. Patiño, J. Llop, S. Sánchez, *Adv. Intell. Syst.* **2020**, *2*.
[16] K. Yuan, B. Jurado-Sánchez, A. Escarpa, *Angew. Chem. – Int. Ed.* **2021**, *60*, 4915.
[17] J. Ou, K. Liu, J. Jiang, D. A. Wilson, L. Liu, F. Wang, S. Wang, Y. Tu, F. Peng, *Small* **2020**, *16*, 1906184.
[18] B. Wang, K. Kostarelos, B. J. Nelson, L. Zhang, *Adv. Mater.* **2021**, *33*, 2002047.
[19] Q. Wang, L. Zhang, *ACS Nano* **2021**, *15*, 149.
[20] P. Wrede, O. Degtyaruk, S. K. Kalva, X. L. Deán-Ben, U. Bozuyuk, A. Aghakhani, B. Akolpoglu, M. Sitti, D. Razansky, *Sci. Adv.* **2022**, *8*, eabm9132.
[21] U. Bozuyuk, E. Suadiye, A. Aghakhani, N. O. Dogan, J. Lazovic, M. E. Tiryaki, M. Schneider, A. C. Karacakol, S. O. Demir, G. Richter, M. Sitti, *Adv. Funct. Mater.* **2022**, *32*, 2109741.
[22] L. Xu, F. Mou, H. Gong, M. Luo, J. Guan, *Chem. Soc. Rev.* **2017**, *46*, 6905.
[23] S. G. Ullattil, M. Pumera, *Small* **2023**, *19*, 2301467.
[24] H. Eskandarloo, A. Kierulf, A. Abbaspourrad, *Nanoscale* **2017**, *9*, 12218.
[25] H. Zhou, C. C. Mayorga-Martinez, S. Pané, L. Zhang, M. Pumera, *Chem. Rev.* **2021**, *121*, 4999.
[26] X. Z. Chen, M. Hoop, F. Mushtaq, E. Siringil, C. Hu, B. J. Nelson, S. Pané, *Appl. Mater. Today* **2017**, *9*, 37.
[27] V. de la Asunción-Nadal, C. Franco, A. Veciana, S. Ning, A. Terzopoulou, S. Sevim, X. Z. Chen, D. Gong, J. Cai, P. D. Wendel-Garcia, B. Jurado-Sánchez, A. Escarpa, J. Puigmartí-Luis, S. Pané, *Small* **2022**, *18*, 2203821.
[28] F. Soto, E. Karshalev, F. Zhang, B. Esteban Fernandez de Avila, A. Nourhani, J. Wang, *Chem. Rev.* **2022**, *122*, 5365.
[29] Z. Xiao, S. Duan, P. Xu, J. Cui, H. Zhang, W. Wang, *ACS Nano* **2020**, *14*, 8658.
[30] J. Wang, X. Liu, Y. Qi, Z. Liu, Y. Cai, R. Dong, *Chem. Eng. J.* **2021**, *416*, 129091.
[31] A. Aziz, J. Holthof, S. Meyer, O. G. Schmidt, M. Medina-Sánchez, *Adv. Healthcare Mater.* **2021**, *10*, 2101077.
[32] J. Li, C. C. Mayorga-Martinez, C. D. Ohl, M. Pumera, *Adv. Funct. Mater.* **2022**, *32*, 2102265.
[33] J. Vyskočil, C. C. Mayorga-Martinez, E. Jablonská, F. Novotný, T. Ruml, M. Pumera, *ACS Nano* **2020**, *14*, 8247.
[34] H. Ceylan, I. C. Yasa, O. Yasa, A. F. Tabak, J. Giltinan, M. Sitti, *ACS Nano* **2019**, *13*, 3353.
[35] H. Ceylan, J. Giltinan, K. Kozielski, M. Sitti, *Lab Chip* **2017**, *17*, 1705.
[36] M. Ussia, M. Urso, M. Kratochvilova, J. Navratil, J. Balvan, C. C. Mayorga-Martinez, J. Vyskocil, M. Masarik, M. Pumera, *Small* **2023**, *19*, 2208259.
[37] X. Peng, M. Urso, M. Pumera, *npj Clean Water* **2023**, *6*, 21.
[38] M. Urso, M. Ussia, M. Pumera, *Nat. Rev. Bioeng.* **2023**, *1*, 236.
[39] J. V. Vaghasiya, C. C. Mayorga-Martinez, S. Matějková, M. Pumera, *Nat. Commun.* **2022**, *13*, 1026.
[40] M. Ussia, M. Urso, S. Kment, T. Fialova, K. Klima, K. Dolezelikova, M. Pumera, *Small* **2022**, *18*, 2200708.
[41] M. Urso, M. Ussia, F. Novotný, M. Pumera, *Nat. Commun.* **2022**, *13*, 3573.
[42] Y. S. Kochergin, K. Villa, F. Novotný, J. Plutnar, M. J. Bojdys, M. Pumera, *Adv. Funct. Mater.* **2020**, *30*, 2002701.
[43] K. Villa, C. L. Manzanares Palenzuela, Z. Sofer, S. Matějková, M. Pumera, *ACS Nano* **2018**, *12*, 12482.
[44] K. Hou, Y. Zhang, M. Bao, C. Xin, Z. Wei, G. Lin, Z. Wang, *ACS Appl. Mater. Interfaces* **2022**, *14*, 3825.
[45] X. Yan, Q. Zhou, M. Vincent, Y. Deng, J. Yu, J. Xu, T. Xu, T. Tang, L. Bian, Y. X. J. Wang, K. Kostarelos, L. Zhang, *Sci. Robot.* **2017**, *2*, eaaq1155.
[46] A. Aziz, S. Pane, V. Iacovacci, N. Koukourakis, J. Czarske, A. Menciassi, M. Medina-Sánchez, O. G. Schmidt, *ACS Nano* **2020**, *14*, 10865.
[47] M. Yang, X. Guo, F. Mou, J. Guan, *Chem. Rev.* **2023**, *123*, 3944.
[48] J. Li, P. Angsantikul, W. Liu, B. Esteban-Fernández de Ávila, S. Thamphiwatana, M. Xu, E. Sandraz, X. Wang, J. Delezuk, W. Gao, L. Zhang, J. Wang, *Angew. Chem. – Int. Ed.* **2017**, *56*, 2156.
[49] B. E. F. De Ávila, P. Angsantikul, J. Li, M. Angel Lopez-Ramirez, D. E. Ramírez-Herrera, S. Thamphiwatana, C. Chen, J. Delezuk, R. Samakapiruk, V. Ramez, L. Zhang, J. Wang, *Nat. Commun.* **2017**, *8*, 272.
[50] B. E. F. De Ávila, P. Angsantikul, J. Li, W. Gao, L. Zhang, J. Wang, *Adv. Funct. Mater.* **2018**, *28*, 1705640.
[51] Y. Liu, G. Lin, G. Bao, M. Guan, L. Yang, Y. Liu, D. Wang, X. Zhang, J. Liao, G. Fang, X. Di, G. Huang, J. Zhou, Y. Y. Cheng, D. Jin, *ACS Nano* **2021**, *15*, 19924.
[52] P. Sudhakar, T. P. Radhakrishnan, *Chem. – An Asian J.* **2019**, *14*, 4754.
[53] A. Patra, T. P. Radhakrishnan, *Chem. – A Eur. J.* **2009**, *15*, 2792.
[54] P. Srujana, P. Sudhakar, T. P. Radhakrishnan, *J. Mater. Chem. C* **2018**, *6*, 9314.
[55] N. Senthilnathan, K. Gaurav, C. Venkata Ramana, T. P. Radhakrishnan, *J. Mater. Chem. B* **2020**, *8*, 4601.
[56] N. Senthilnathan, C. G. Chandaluri, T. P. Radhakrishnan, *Sci. Rep.* **2017**, *7*, 10583.
[57] P. Gayathri, M. Pannipara, A. G. Al-Sehemi, D. Moon, S. P. Anthony, *Mater. Adv.* **2021**, *2*, 996.
[58] J. Mei, N. L. C. Leung, R. T. K. Kwok, J. W. Y. Lam, B. Z. Tang, *Chem. Rev.* **2015**, *115*, 11718.
[59] C. M. Oral, M. Ussia, M. Urso, J. Salat, A. Novobilsky, M. Stefanik, D. Ruzek, M. Pumera, *Adv. Healthcare Mater.* **2023**, *12*, 2202682.
[60] H. Xie, M. Sun, X. Fan, Z. Lin, W. Chen, L. Wang, L. Dong, Q. He, *Sci. Robot.* **2019**, *4*, eaav8006.
[61] A. C. Hortelao, C. Simó, M. Guix, S. Guallar-Garrido, E. Julián, D. Vilela, L. Rejc, P. Ramos-Cabrer, U. Cossío, V. Gómez-Vallejo, T. Patiño, J. Llop, S. Sánchez, *Sci. Robot.* **2021**, *6*, eabd2823.
[62] Y. W. Jun, H. R. Kim, Y. J. Reo, M. Dai, K. H. Ahn, *Chem. Sci.* **2017**, *8*, 7696.
[63] S. K. Lai, Y. Y. Wang, J. Hanes, *Adv. Drug Delivery Rev.* **2009**, *61*, 158.